Int. J. Heat Mass Transfer. Vol. 34, No. 4/5, pp. 1175–1187, 1991
Printed in Great Britain

0017–9310/91 $3.00+0.00
© 1991 Pergamon Press plc

Heat transfer enhancement of laminar and turbulent pipe flow via corona discharge

M. M. OHADI,† D. A. NELSON and S. ZIA
Mechanical Engineering–Engineering Mechanics Department,
Michigan Technological University, Houghton, MI 49931, U.S.A.

(*Received* 9 *October* 1989 *and in final form* 19 *June* 1990)

Abstract—The effect of corona discharge on forced-convection heat transfer in a tube is studied experimentally. Results are reported for parametric values of the Reynolds number (1000–15 000), electric field potential (0 kV to near spark-over potential), and number of electrodes (single or double electrode configurations). The working fluid in all experiments is air. It is found that heat transfer enhancements are significant only in the laminar and transitional flow regimes when using a single electrode. On the other hand, with a two-electrode configuration, enhancements extend to the turbulent flow regime as well. At constant pumping power higher enhancements are generally associated with the double electrode configuration. The only exception to this is for the fully laminar Reynolds numbers and at the highest field potentials, where the single electrode results exceed those of the double electrode.

INTRODUCTION

IT HAS long been established that coupling of an electric field with a flow field (the so-called electrohydrodynamic, or EHD effect) can significantly affect convective heat and mass transfer rates [1–5]. Broadly speaking, the flow produced by applying a d.c. electric field to a weakly-ionized fluid (the 'corona wind') may be pictured as a free jet discharged into a fluid of the same type [5]. The net effect of the primary corona wind and the secondary flows it may create can be used to destabilize the thermal boundary layer on the heat transfer wall and therefore enhance the heat transfer coefficient.

The electric body force which gives rise to generation of the corona wind effect in a homogeneous dielectric is given as [6]

$$\mathbf{F}_e = \rho_c \mathbf{E} - \tfrac{1}{2}E^2\nabla\varepsilon + \tfrac{1}{2}\nabla\left[E^2\rho\left(\frac{\partial\varepsilon}{\partial\rho}\right)_T\right] \qquad (1)$$

where $\mathbf{F}_e$ is the electric body force, $\mathbf{E}$ the electric field potential, ρ and ρ_c the mass density and space-charge density, respectively, ε the gas permittivity and T the temperature.

In cases where the permittivity of the fluid is assumed constant, the second and third terms on the right-hand side of equation (1) become negligible. In such cases, the electric body force is simply the Coulombic force

$$\mathbf{F}_e = \rho_c \mathbf{E}. \qquad (2)$$

Yabe *et al.* [7] demonstrated that the Coulombic force was the principal force in producing corona wind for positive discharge in a wire-and-plate geometry, with nitrogen as the working fluid.

The working fluid in all of the present study experiments was air at steady-state conditions. The results reported in this paper correspond to a positive electrode field potential. The effect of field polarity and flow visualization studies will be the subjects of a forthcoming publication. A schematic view of the physical situations to be studied here is presented in Figs. 1(a) and (b). In Fig. 1(a) a high voltage (d.c.) electric field is applied to a single co-axial electrode. The set-up shown in Fig. 1(b) differs from that of Fig. 1(a) in that the single concentric electrode is replaced with two electrodes symmetrically positioned from the tube central axis. The experiments were performed as a function of three parameters: (1) the pipe-flow Reynolds number Re, which ranged from about 1000 to 20 000 for the single electrode case and from 1000 to 10 000 for the two-electrode case, (2) the electrode potential, the values of which were 0, 6.50, 7.00, and 7.75 kV for the single electrode case and 0, 7.00, 7.25, 7.50, and 7.75 kV for the double electrode case, and (3) electrode configurations (single and double electrode arrangements as shown in Figs. 1(a) and (b), respectively). For both the single and double electrode configurations, the 0 kV field experiments correspond to the absence of the electric field, so that they served as a baseline against which the with-field results are compared.

The literature on electrohydrodynamic (EHD) enhancement of heat and mass transfer include applications to both external and internal (duct) flows.

† Present address: Department of Mechanical Engineering, University of Maryland, College Park, MD 20742, U.S.A.

NOMENCLATURE

A	heat transfer surface area
c_p	specific heat at constant pressure
d	test section tube inner diameter
E	electric field potential
E_T	electric field at threshold potential
E_M	electric field at maximum potential
F_e	electric field body force
$\bar{h}$	average heat transfer coefficient
i_t	electric current for the entire length of electrode
J	current density
k	thermal conductivity
l	electrode length in the heat transfer test section
l_t	total electrode length
$\dot{m}$	mass flow rate
Nu	Nusselt number, equation (10)
Q_{G1}	heating energy supply to inlet guard heater
Q_{G2}	heating energy supply to exit guard heater
$Q_{C,G1}$	corona heat dissipation to inlet guard heater
$Q_{C,G2}$	corona heat dissipation to exit guard heater
Q_L	heat loss from the test section
$Q_{L,G1}$	heat loss from inlet guard heater
$Q_{L,G2}$	heat loss from exit guard heater
Q_S	heat supplied to the test section
Q_{SC}	corona heat dissipation to the test section
Q_{Sr}	resistive heating to the test section
R_L	overall thermal insulation resistance
Ra	Rayleigh number
Re	Reynolds number, $4\dot{m}/\mu\pi d$
$\bar{T}_b$	average flow bulk temperature
T_{bA}	bulk temperature at inlet of the first guard heater
T_{bB}	bulk temperature at test section inlet
T_{bC}	bulk temperature at test section exit
T_{bD}	bulk temperature at the exit of second guard heater
$\bar{T}_w$	average wall temperature
$\bar{T}_{w0}$	average temperature at the test section outer wall
T_∞	ambient (here laboratory) temperature
U	nominal fluid velocity
W_p	pumping power.

Greek symbols

β	ion mobility
ε	gas permittivity
μ	viscosity
ξ	dimensionless electric field current
ρ	mass density
ρ_c	charge density
φ	dimensionless electric field potential.

Subscripts

b	bulk
C	corona, also charge
G	guard heater
L	loss
M	maximum
t	total
T	threshold
S	supplied
w	wall.

Most of the work reported has been experimental. However, limited theoretical work has been conducted as well. In general, past work establishes that EHD effects are most significant in situations where flow is in the laminar, up to transitional, regime. For highly turbulent flows the electrically-induced effects become swamped in the presence of turbulence-induced eddy diffusivity effects. A thorough review of literature on EHD enhancement of convective heat and mass transfer is documented in ref. [8]. As indicated there, although there exists a large body of literature on EHD-related heat transfer augmentation, studies on forced convection in gases are limited. The only study with conditions partially corresponding to those experimented here appears to be the work by Velkoff [1] who studied EHD effects on heat transfer enhancements and pressure drop characteristics for a wire in a tube configuration, using air as the working fluid. However, Velkoff's experiments included only use of a single electrode and over a limited range of Reynolds number and electric field potential. With respect to general studies on EHD heat/mass transfer enhancements, examples include the work by Franke and Hutson [9] who examined the effect of corona discharge on free convection heat transfer coefficients in a heated vertical cylinder. Mizushina *et al.* [10] conducted experiments on EHD augmented forced convection in an annulus with air as the working fluid. Both positive and negative field polarities were examined. Augmented Nusselt numbers and friction factors were correlated in terms of the ratio of ion-drag forces to viscous forces in the bulk flow. The developed correlation was found to work well for laminar flows, but failed to correlate in the turbulent flow range. More recently, Fujino *et al.* [11] studied augmentation of laminar forced convection heat transfer in a channel flow by a transverse (d.c.) electric field with refrigerant 113 (R113) as the working fluid. The walls of the parallel-plate channel served as the electrodes, one of which was used as a

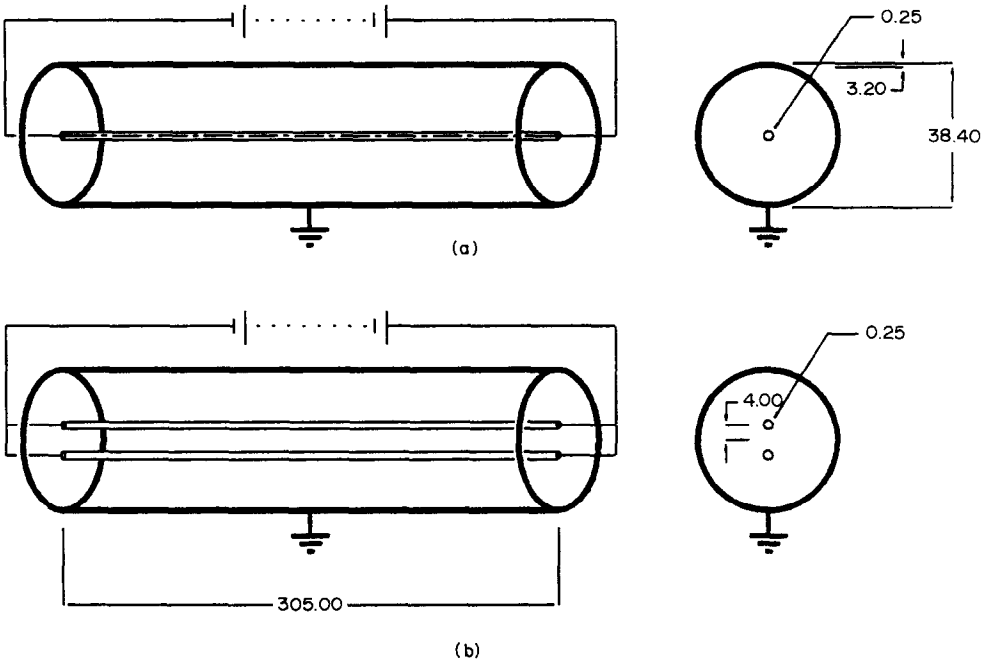

All dimensions in mm.

FIG. 1. Schematic representation of the two investigated electrode and tube systems.

heat transfer surface of uniform heat flux. The effects of both positive and negative field polarities were studied.

Interest in applying EHD effects to enhance heat transfer in heat exchangers has begun to appear in the literature as well. Yabe *et al.* [12] reported a 280% increase in condensation heat transfer through the use of helical electrodes outside vertical tubes. Recent studies in the U.K. have demonstrated heat transfer enhancements of as much as a factor of 23 in geometries of practical interest using industrial fluids such as transformer oil, aircraft fuel, hexane, silicone oil, etc. This body of work includes the studies by Chang *et al.* [13], Cooper and Allen [14, 15], Poulter and Miller [16], and Poulter and Allen [17].

EXPERIMENTAL APPARATUS AND PROCEDURE

Experimental apparatus

Both heat transfer and pressure drop experiments were performed during the course of the present investigation. This paper will report the heat transfer results and the corresponding pressure drop effects in terms of pumping power requirements. As depicted in Fig. 2, the heat transfer experimental apparatus consisted of three main segments: (1) the heat transfer test section and its corresponding heating energy supply circuitry, (2) the high-voltage circuitry and electrode tensioning mechanism, and (3) the air handling system. Brief descriptions of these segments will be given in the following sections, with details available in ref. [8].

Heat transfer test section. The heat transfer test section was an assembly of several components, as depicted in Figs. 2 and 3. It consisted of a central portion (the heated test section) flanked at either end by a guard heater coupled to the inlet or exit sections. The inlet guard heater, the heated test section and the exit guard heater are shown as portions AB, BC, and CD, respectively, in Fig. 3. The heat transfer test section and the guard heaters at its respective ends were made of aluminum (6061-T6) tubing with inner and outer diameters of 3.2 cm (1.25 in.) and 3.8 cm (1.50 in.), respectively. The length of the heated test section was 30.5 cm (12 in.) while that of each guard heater was 9.2 cm (3.62 in.).

Heating of both the test section and guard heaters was accomplished by resistive heating in the tube wall via a d.c. power supply. Circumferential grooves, 1.80 mm (0.068 in.) wide and 2.38 mm (0.093 in.) deep having a pitch of 7 threads $in.^{-1}$, were machined in the outer wall of the test section tube. A nichrome heating ribbon (1.60 mm × 0.127 mm, ohmic rating of 0.589 mm^{-1} length) was installed in the heated test section and guard heater sections. Electrical insulation of the heating ribbon from grooved channels was provided by use of a special high temperature electrical insulation tape which was carefully wrapped around the test section tube. Six pre-calibrated, gage 30 chromel–constantan thermocouples were installed in the test

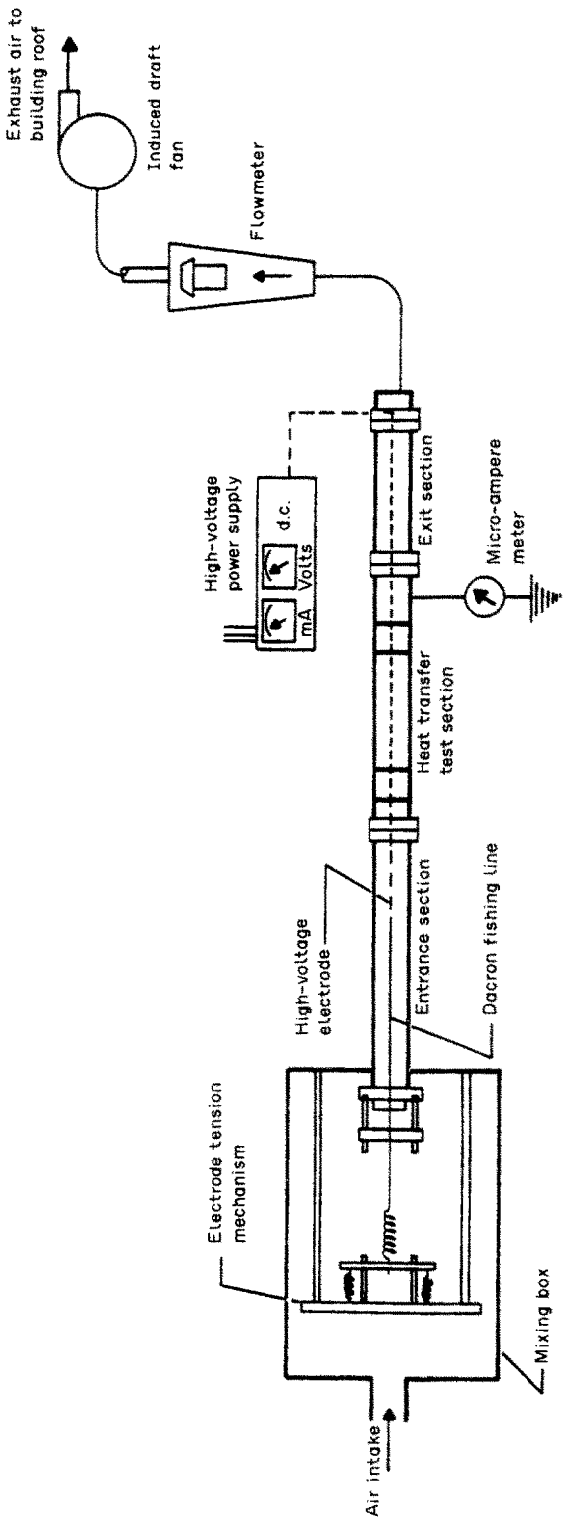

FIG. 2. Schematic representation of the experimental heat transfer apparatus setup.

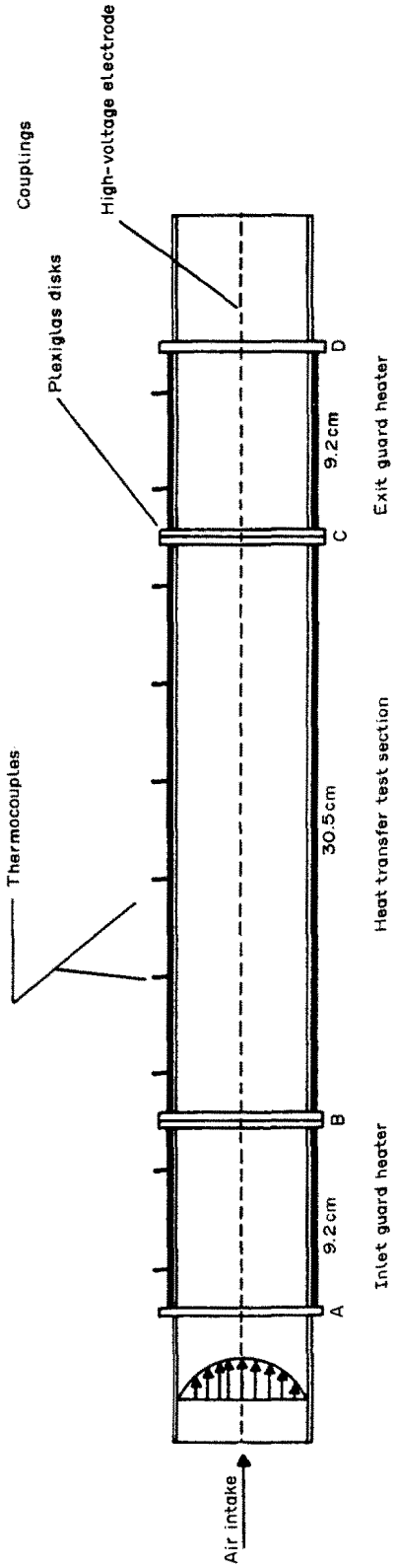

FIG. 3. Schematic representation of the heat transfer test section.

section. Each guard heater was equipped with two thermocouples, as shown in Fig. 3. The thermocouples were equally spaced at intervals of 5 cm (≈ 2 in.). The thermocouple junctions were positioned at 0.8 mm (0.031 in.) from the inner surface of the tube wall that was exposed to the air flow. Prior to inserting the thermocouples in their respective holes, the junction beads were dipped in a special high thermal conductivity paste which served to reduce the thermal contact resistance between the thermocouple and the tube wall. The thermocouples were kept in position with a silicone adhesive compound.

To minimize extraneous conduction losses from the test section, the heat transfer test section heater and the respective guard heaters were fabricated with separate heating circuits, thereby making them separately controllable. During each experiment, the temperatures of the adjacent portions of the test section and the guard heaters were matched by balancing the readings of suitably positioned thermocouples. To increase the sensitivity of the temperature-matching procedure, insulating spacers made of Plexiglas were positioned between the respective ends of the test section and the guard heaters.

Corona discharge. Corona discharge to the air was through a wire electrode(s) which was connected to a high voltage (0–30 kV), low current (0–15 mA), low ripple d.c. power supply. The electrode was made of stainless steel (AISI 304) with a wire diameter of 0.25 mm (≈ 0.01 in.). It ran the length of the heat transfer test section and extended 34 cm (equivalent of 10.7 tube inner diameters) into the inlet and exit sections. This precaution was needed to minimize any electric field end effects at the ends of the heat transfer test section. At the upstream end, the electrode(s) was joined to a braided dacron fishing line, tested for tensile strength of 89 N. To eliminate any residual kinks or nonuniformity in the wire, each electrode was 'aged' under tension for several hours prior to installation.

The joint between the dacron fishing line and the stainless steel electrode was sufficiently fine to minimize any flow disturbance. This was achieved by running the electrode wire into the fishing line to a depth of ≈ 2.54 cm (1 in.) and use of a special adhesive bond. The strength of the joint was tested to about 35.6 N (8 lb_f) without breakdown, while the electrode tensioning mechanism only required 11.1 N (2.5 lb_f) tensioning force. The use of dacron fishing line at the upstream end of the electrode was a safety feature for the system as it isolated the live parts of the high voltage assembly from the easy to access/exposed system components.

The tensioning mechanism of the electrode to assure safe and reliable system operation was a major component of the experimental apparatus. A schematic of the final design is shown in Fig. 2. It consists of three main components: (1) two aluminum bars, (2) two linear brush bearing and shafts, and (3) two pre-calibrated tensioning springs. It was determined (by calculation and experimental verification) that a tensioning force of 11.1 N (2.5 lb_f) would provide a sag-free tensioning of the electrode for the present study experiments. As was pointed out earlier, the system was tested for forces up to 35 N. The spring-loaded design allowed varying tension for the electrode by adjusting the knobs attached to the tensioning springs.

Air handling system. Flow delivery to the test section was via an inlet section tube, made of aluminum 6061-T6, with inner and outer diameters the same as those of the heat transfer and guard heater sections. The finished length of the delivery tube was 160 cm (equivalent to 50 tube diameters). This length was sufficient to allow hydrodynamic development of the flow before entering the test section. Downstream of the test section, an exhaust tube continued the test section's 3.175 cm (1.250 in.) internal diameter for a length of about 13 diameters. Thereafter, the piping was connected to a 5.08 cm (2.0 in.) diameter PVC tubing appropriate to the rotameters used for measurement of the mass flow rate. Various rotameters were used depending on the magnitude of the flow. After the rotameters, the flow passed through a control valve and was then ducted to a blower.

As a by-product, the process of corona discharge in air results in generation of ozone (O_3) under certain operating conditions. This gas is known to be hazardous to health when present at high concentrations. As shown in Fig. 2, the exhaust of the apparatus system was vented outdoors to avoid exposure to ozone. The downstream positioning of the blower avoided preheating of the air entering the apparatus. To prevent the blower from heating the laboratory space, the blower was housed inside a well-insulated drum. Proper auxiliary cooling for the enclosed blower ensured its safe operation within the manufacturer's specified conditions.

Experimental procedure

Execution of a heat transfer experiment involved a number of steps. First air flow was activated through the apparatus by turning on the system blower. Next, the building exhaust fan which delivered exhaust of the apparatus to the building roof was switched on. The power supply to the heated test section and guard heaters was then turned on and set at pre-determined levels for the given run. The set values were based on the criteria that the temperature difference between the tube wall and the bulk flow ($T_w - T_x$) was not to exceed ≈ 20°C. This temperature limit was low enough to make buoyancy effects negligible.

The test section and guard heaters were then allowed to reach their thermal equilibrium conditions. This usually took about 45–60 min, depending on the Reynolds number. After steady-state conditions were reached, the temperature readings from the heated test sections were compared with those of the corresponding adjacent guard heaters. Any necessary adjustments in the power supplied to the guard heaters

were made until a temperature difference of less than 0.1°C between the respective test section ends and the guard heaters was achieved. The total time for thermal equilibrium of the system, including the initial warm up period, was about 3 h on the average. After establishing the thermal equilibrium conditions, the data collection process was started, using a computer assisted data acquisition system.

DATA REDUCTION

Average heat transfer coefficient

The main objective of the data reduction was to evaluate the average heat transfer coefficient and Nusselt number under a given Reynolds number and electric field potential. The average heat transfer coefficient was determined by introducing the experimental data into the defining equation

$$\bar{h} = (Q_S - Q_L)/[(\bar{T}_w - \bar{T}_b)A] \tag{3}$$

in which Q_S and Q_L, respectively, correspond to the energy supplied and the heat losses from the test section at average wall temperature $\bar{T}_w$ and fluid bulk temperature $\bar{T}_b$. The quantity A is the heat transfer surface area.

The power supplied to the test section Q_S was from two sources: resistive heating from the nichrome ribbon and the heat dissipation associated with corona discharge

$$Q_S = Q_{Sr} + Q_{Sc}. \tag{4}$$

The power supplied by the heating element Q_{Sr} is simply the product of the measured current and voltage. Heat dissipation due to corona discharge in the test section, on the other hand, could not be determined directly and had to be approximated as

$$Q_{Sc} = \left(i_t \frac{l}{l_t}\right) E \tag{5}$$

where i_t is the total measured current for the entire length of the electrode l_t. That portion of the electrode length which spans the heated test section (section BC in Fig. 3) is denoted by l while the high voltage electric field potential drop across the electrodes is shown as E. Equation (5) assumes that the current density is uniform along the length of the electrode. This was a reasonable assumption considering that the heat dissipation due to corona was a small quantity (of the order of 1 W or less) due to very small current flows ($\approx$ 1 mA or less).

The heat loss from the test section Q_L was due to two mechanisms: axial conduction along the tube length and natural convection from the outer surface of the test section. Axial conduction losses were made negligible by the presence of a guard heater at each end of the test section. Convection losses were minimized by a 5 cm (2.0 in.) layer of fiberglass insulation around the test section tube. By mounting a thermocouple at the outer surface of the insulation, convection losses were estimated as

$$Q_L = \frac{\bar{T}_{w0} - T_\infty}{R_L} \tag{6}$$

where T_{w0} and T_∞ refer to temperatures at the outer surface of the test section wall and that corresponding to the laboratory environment, respectively. The quantity R_L is the thermal resistance due to the cylindrical insulation layer and the natural convection from the outer surface of the insulation to still air (laboratory air).

Average fluid bulk temperature $\bar{T}_b$

Calculation of the heat transfer coefficient in equation (3) required knowledge of both $\bar{T}_w$ and $\bar{T}_b$. The average wall temperature $\bar{T}_w$ was taken as the mean of the six axial thermocouples which were equally spaced along the test section tube wall. Direct measurement of the fluid bulk temperature $\bar{T}_b$ in the presence of a high-voltage field, on the other hand, was not possible for two reasons. First, the output signal of thermocouples for the present study experiments was only a few millivolts and would have easily been swamped in the presence of the high-voltage field (over 7500 V in the present study experiments). The second major problem with direct temperature measurement was that introducing a pointed object such as a thermocouple into the electric field would result in local distortion of the electric field. Any distortion of the field would alter the local electrostatic force on the fluid—thus altering the heat transfer rates.

The fluid bulk temperature, therefore, had to be determined by an energy balance (first law) analysis. Referring to Fig. 3 the average fluid bulk temperature was taken as the means of inlet and exit bulk temperatures, T_{bB} and T_{bC}, respectively

$$\bar{T}_b = \frac{T_{bB} + T_{bC}}{2} \tag{7}$$

in which T_{bB} and T_{bC} refer to temperatures at positions B and C in Fig. 3.

The bulk temperature at the inlet to the test section was found by an energy balance on the inlet guard heater

$$T_{bB} = T_{bA} + \frac{Q_{G1} + Q_{C,G1} - Q_{L,G1}}{\dot{m}C_p}. \tag{8}$$

Similarly an energy balance on the second guard heater yielded the exit bulk temperature as

$$T_{bC} = T_{bD} + \frac{Q_{G2} + Q_{C,G1} - Q_{L,G2}}{\dot{m}C_p} \tag{9}$$

where Q_{G1} and Q_{G2} are the power supply to inlet and exit guard heaters, respectively, $Q_{C,G1}$ and $Q_{C,G2}$ the corona-induced heat dissipation to the two guard heaters, respectively, and $Q_{L,G1}$ and $Q_{L,G2}$ the heat loss from the two guard heaters, respectively.

All the quantities on the right-hand side of equations (8) and (9) were either measured directly or calculated indirectly as outlined in earlier sections. Having found the heat transfer coefficient from equations (4) to (9), the Nusselt number was calculated as

$$\overline{Nu} = \bar{h}d/k \tag{10}$$

in which d is the test section tube inner diameter and k the thermal conductivity of the working fluid (here air). The Reynolds number used in parameterization of heat transfer results was evaluated from

$$Re = 4\dot{m}/\mu\pi d \tag{11}$$

where $\dot{m}$ is the measured mass flow rate and μ was evaluated for pure air.

RESULTS AND DISCUSSION

Single electrode results

Presentation of the results will begin with data corresponding to the single electrode case which are presented in Figs. 4–7. Attention is first directed to Fig. 4 which depicts a current vs voltage ('I–V') plot for both single and double electrodes at a Reynolds number of 10000. Prior to planning the experiments, it was necessary to generate I–V plots to determine the threshold and spark-over potentials. The threshold voltage corresponds to the voltage at the onset of corona discharge (experimentally, the first non-zero current reading on the ammeter in Fig. 2). The spark-over voltage refers to the voltage just prior to the electrical breakdown of the dielectric (experimentally, the voltage just prior to observing sparks in the air gap between the electrode and the tube wall). For the single electrode, the threshold and spark-over voltages plotted in Fig. 4 are approximately 6.5 kV (with the corresponding current of 6.6 μA) and 7.75 kV (with the corresponding current of 385 μA), respectively.

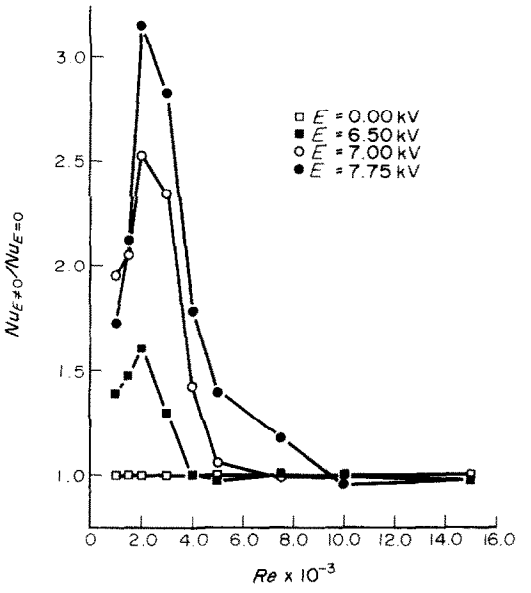

FIG. 5. Effect of Reynolds number on heat transfer enhancements at different field potentials.

Attention will next be directed to Fig. 5 which presents heat transfer enhancements as a function of Reynolds number for the four investigated electrode potentials. To provide a direct comparison, heat transfer enhancements are expressed as the ratio of Nusselt numbers in the presence of an applied electric potential ($Nu_{E\neq0}$) to those with no applied electric field ($Nu_{E=0}$). With the no-electric field experiments

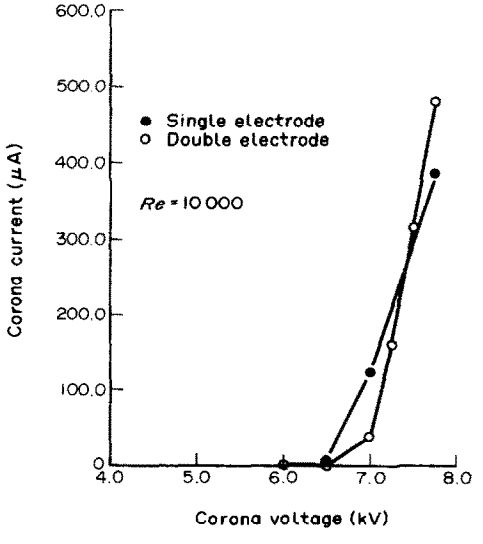

FIG. 4. 'I–V' plots for single and double electrode configurations at Re = 10000.

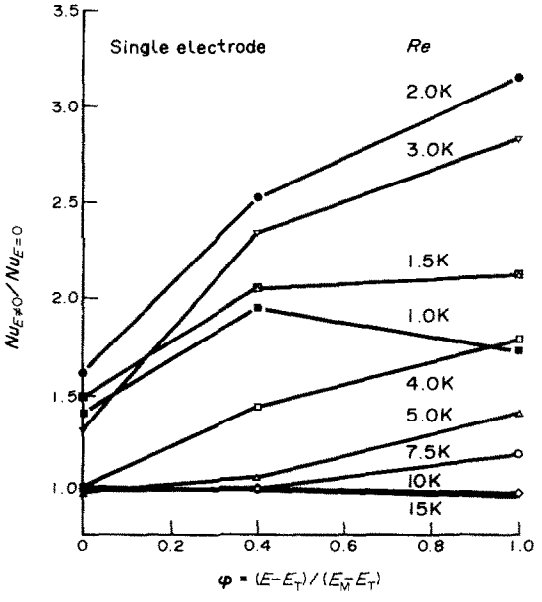

FIG. 6. Heat transfer enhancements as a function of dimensionless field potential, single electrode.

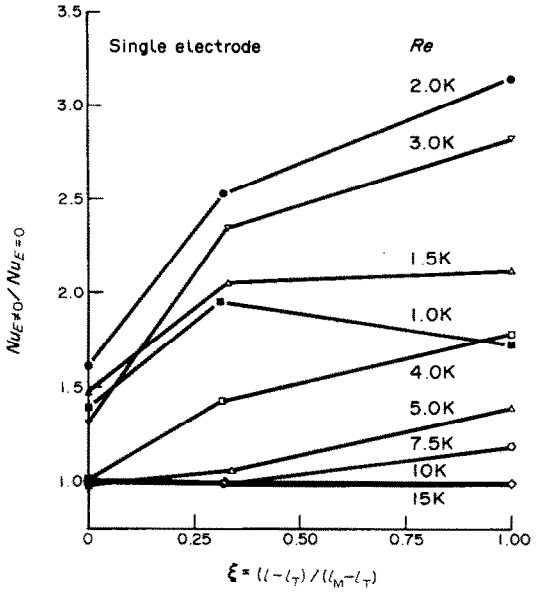

FIG. 7. Heat transfer enhancements as a function of dimensionless current, single electrode.

serving as the base case, the enhancement ratios ($Nu_{E\neq0}/Nu_{E=0}$) should be free of any systematic errors in the experimental apparatus and procedure. Using the Kline–McClintock method [18] the overall uncertainty for the reported Nusselt numbers was calculated to be $\pm 11.5\%$.

From an overall inspection of the results in Fig. 5 two general characteristics can be identified. First, higher applied electric field potentials lead to higher enhancements for flows in the transitional and turbulent regimes. The maximum enhancement in Fig. 5 is 215% and it takes place at $E = 7.75$ kV and $Re = 2000$. Second, enhancements are most significant at Reynolds numbers close to transitional values (here $Re \approx 2000$). As the Reynolds numbers extend into the turbulent regime, lower enhancements are observed until for $Re \geqslant 10\,000$, no enhancements are observed even at the maximum applied potential.

A more direct presentation of voltage and current effects on heat transfer enhancements is given in Figs. 6 and 7. The abscissa of Fig. 6 is dimensionless voltage and that of Fig. 7 is dimensionless current. The subscripts T and M, respectively, refer to the threshold and maximum electrode potentials. Attention is first focused on Fig. 6 which presents heat transfer enhancements as a function of dimensionless field potential. From an overview of the results in Fig. 6 it is clear that higher enhancements are observed for transitional and moderately turbulent Reynolds numbers as field potential increases. Here the highest enhancement is 215% and belongs to $Re = 2000$. On the other hand, for highly turbulent flows (here $Re \geqslant 10\,000$) the results in Fig. 6 show that no enhancement is obtained even at the maximum applied electrode potential. This is an indication that the corona-induced secondary motions become overwhelmed by the eddy diffusivity effects associated with a highly turbulent flow. These findings are consistent with the experimental results of Velkoff [1] in which maximum enhancements corresponded to transitional Reynolds numbers and were found to decrease sharply with further increase in Reynolds number. In ref. [1] the maximum enhancement was 100%, occurring at $Re = 3000$. For $Re \geqslant 9000$ virtually no enhancements were present.

For low Reynolds numbers the increase in field potential above a certain level is seen to decrease the heat transfer enhancements. As shown in Fig. 6, for $Re = 1000$ and 1500, increasing the potential beyond $\varphi = 0.4$ (i.e. 40% of the maximum applicable potential) results in lower heat transfer enhancements. This is contrary to the results obtained for the transitional and turbulent Reynolds numbers. Initially it was speculated that the corona-induced Joule heating effect may have introduced buoyancy-driven secondary motions that can cause distortion of the well-defined EHD secondary motions, and thus reduce the enhancement effects. However, calculation of the Rayleigh numbers at $Re = 1000$ and 1500 indicated a value of $\approx 3 \times 10^4$, suggesting a forced convection mode according to the criteria established in ref. [19]. The physical model of Moss and Gray [20] may be used to explain the observed trend. According to their model, electrically-induced secondary motions are most effective at intermediate field potentials. As shown in Fig. 8, at the maximum corona discharge the electrically-induced recirculating regions of the flow are substantially reduced, leading to reduction in EHD heat transfer enhancements.

The results depicted in Fig. 7 suggest that the enhancement is current dependent. This is evident from Ohm's law

$$\mathbf{J} = \beta|\rho_c|\mathbf{E} + \rho_c\mathbf{U} \tag{12}$$

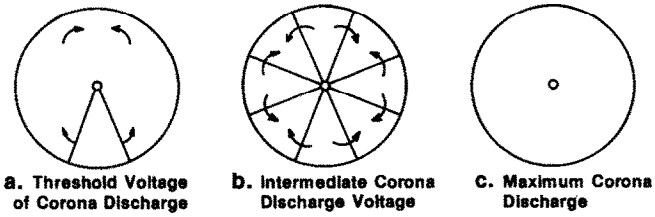

FIG. 8. Hydrodynamics of EHD—augmentation in tube flow [21].

where **J**, **E** and **U** are the vectors for current density, electric field potential, and fluid velocity. The quantities β and ρ_c are the ion mobility and charge density, respectively. The total current is therefore composed of two components: that due to electrophoretic effects, $\beta|\rho_c|\mathbf{E}$, and that due to convective transport of charge, $\rho_c\mathbf{U}$. For situations where convection contribution to the total current is negligible, equation (12) requires that

$$\frac{U}{\beta E} \ll 1 \tag{13}$$

where U and E are nominal fluid bulk velocity and electric field magnitudes, respectively. For present study experiments the convective contributions to total current were shown to be much smaller than the electrophoretic contributions [8]. Therefore, for positive charge carriers, the current density reduces to

$$\mathbf{J} = \beta\rho_c\mathbf{E}. \tag{14}$$

Comparison of equations (3) and (14) shows that the electric body force is related to the current density by

$$\mathbf{F}_e = \mathbf{J}/\beta. \tag{15}$$

Thus, the electric body force is proportional to the current density, thereby confirming the trends of the data observed in Fig. 7.

The two-electrode results

The '*I–V*' plot for both the single and double electrode configurations was shown in Fig. 4. For the two-electrode configuration the minimum and maximum potentials for which enhancements were measured are 7.0 kV (with corresponding current of 40 μA) and 7.75 kV (with corresponding current of 480 μA). When compared to those of the single electrode case, it is seen that addition of the second electrode has increased both the threshold and maximum potentials.

Distribution of heat transfer enhancements as a function of dimensionless electric field potential and current for the two-electrode configuration are shown in Figs. 9 and 10, respectively. Careful study of the results and their comparison with Figs. 6 and 7 indicates that the major trends identified for the single electrode hold true for the double electrode case as well. A notable difference, however, is that here the enhancements are maximum at $Re = 3000$, in contrast to $Re = 2000$ for the single electrode case. Furthermore, for both $Re = 1000$ and 2000, an increase in dimensionless field potential beyond $\varphi \approx 0.33$ results in lower enhancements. This compares to a $\varphi = 0.40$ for the single electrode case. Therefore, for the two-electrode case peak enhancements take place at lower field potentials when operating at laminar, up to transition, Reynolds numbers.

Another interesting observation is that, when compared to those of the single electrode (Figs. 6 and 7),

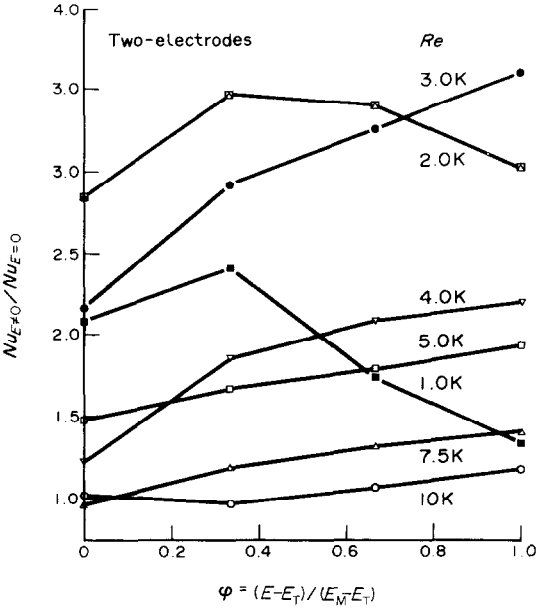

FIG. 9. Heat transfer enhancement as a function of dimensionless field potential, double electrode.

the relative decline in heat transfer enhancements for lower Reynolds numbers, is more pronounced. For $Re = 1000$, and at the maximum field potential, enhancements fall below that of $Re = 7500$, as shown in Fig. 9. The explanation of the observed trend is similar to that offered for the single electrode case. The higher electric field intensity results in more uniform field distribution and therefore reduced EHD effects.

Direct comparison of the single and double elec-

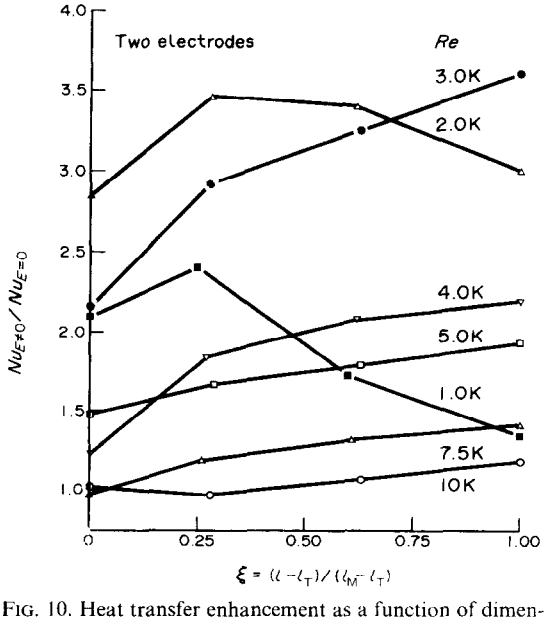

FIG. 10. Heat transfer enhancement as a function of dimensionless current, double electrode.

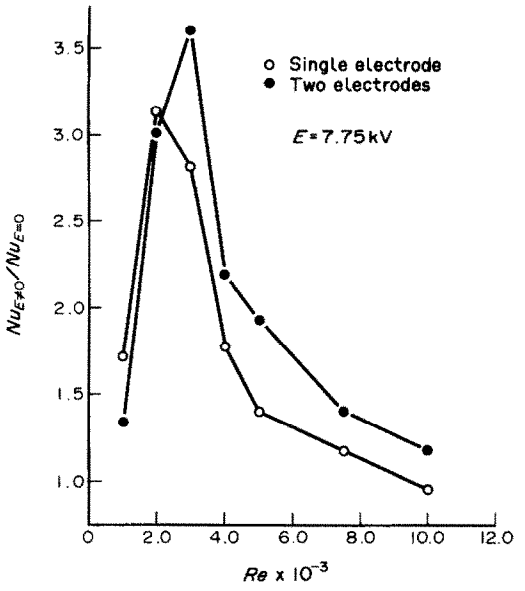

FIG. 11. Comparison of heat transfer enhancements for single and double electrode configurations at $E = 7.75$ kV.

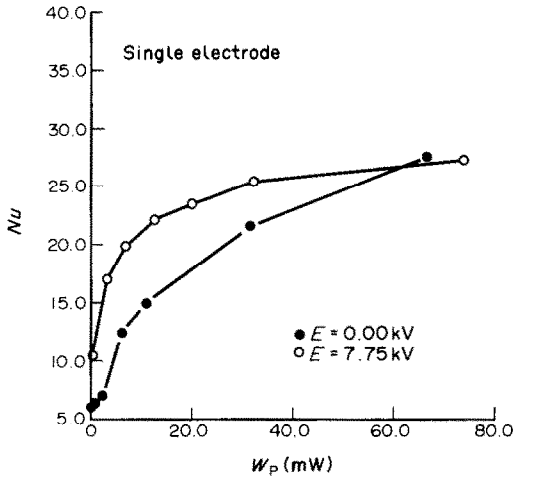

FIG. 12(a). Nusselt number vs pumping power, single electrode.

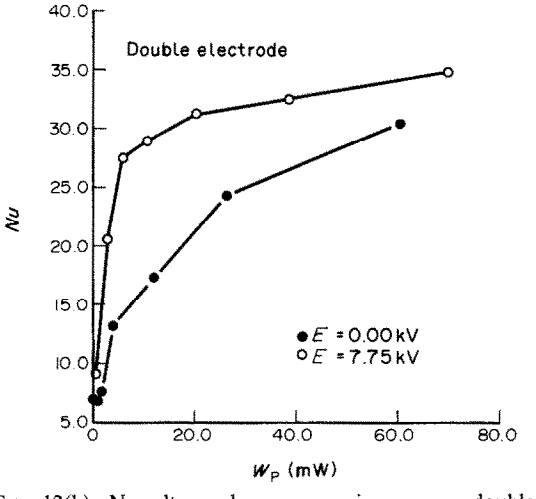

FIG. 12(b). Nusselt number vs pumping power, double electrode.

trode heat transfer enhancements at the maximum experimented field potential ($E = 7.75$ kV) is presented in Fig. 11. As seen there, for $Re > 2000$, enhancements for the double electrode configuration are consistently higher than their respective single electrode enhancements. On the other hand for low Reynolds numbers ($Re \leqslant 2000$), single electrode enhancements out perform those of the double electrode. From the results in Fig. 11, it is also interesting to note that with the two-electrode configuration sizable enhancements are observed even under highly turbulent flow conditions. At $Re = 7500$ and 10 000 enhancements are 41 and 18%, respectively. For the single electrode the corresponding enhancement at $Re = 7500$ was 18% and no enhancement was present at $Re \geqslant 10\,000$.

Pressure drop effects

To evaluate heat transfer enhancements on a constant pumping power basis, the Nusselt numbers are plotted against the pumping power W_p in Figs. 12 and 13. The quantity W_p represents the pumping power required to make the fluid flow in the test section against the pressure drop Δp, as measured between the inlet and exit of the test section. In both Figs. 12(a) and (b), at a given pumping power the difference between the two curves represents heat transfer enhancement on a constant pumping power basis. The results verify the notion that EDH heat transfer enhancement introduces a minimum pressure drop penalty when compared to many other techniques. However, note that, in particular for the single electrode case, the optimum conditions fall in the region of low to moderate power consumption levels. This trend is consistent with their parent enhancement data in Figs. 6 and 9, which suggested that enhancements gradually diminished as Reynolds numbers increased from fully laminar to fully turbulent conditions. Comparison of the results for single and double electrodes (Fig. 13) indicates that, with the exception of fully laminar flows, higher enhancements are consistently associated with the double electrode configuration at a given pumping power.

CONCLUDING REMARKS

The experiments described here have provided definitive information on enhancement of in-tube, single phase convection heat transfer rates of a gas by means of high-voltage electrostatic field with low power consumption. Effects of three parameters were addressed: (1) the flow Reynolds number, which encompassed the range from fully laminar to fully tur-

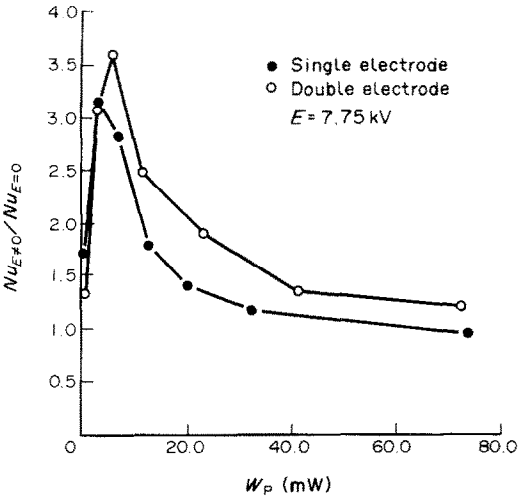

FIG. 13. Comparison of Nusselt number vs pumping power for single and double electrodes.

bulent conditions, (2) the electric field potential, for which results were presented for zero field potential and values in between the threshold and spark-over potentials (with the 0 kV corresponding to the absence of an applied electric field), and (3) number of electrodes (single and double electrode configurations).

It was found that, for both the single and double electrode configurations, highest enhancements take place at Reynolds numbers close to the transitional values (here $Re = 2000$ for the single electrode and $Re = 3000$ for the double electrode configurations). For fully laminar flows enhancements were lower when operating at field potentials close to the spark-over voltages. The decrease in enhancement rates were particularly pronounced for the two-electrode case in which enhancements dropped below those of the single electrode at the highest field potential (7.75 kV). For fully turbulent flows, on the other hand, enhancements essentially increased with increasing field potentials. However, at a given potential, the magnitudes of enhancements decreased with increasing Reynolds numbers. No enhancements were observed for $Re \geqslant 10\,000$ for the single electrode and $Re \geqslant 15\,000$ for the double electrode configurations.

The two-electrode configuration yielded higher enhancements when compared to those of the single electrode. The maximum enhancements obtained for the single electrode was 215% and occurred at $Re = 2000$. The corresponding enhancement for the double electrode was 260% which occurred at $Re = 3000$. On a constant pumping power basis, higher enhancements were associated with the two-electrode configuration at all the Reynolds numbers examined, except for the fully laminar conditions where the single electrode configuration yielded higher enhancements.

Acknowledgements—The support of this work by Gas Research Institute, under contract No. 5087-260-1528, is greatly acknowledged.

REFERENCES

1. H. R. Velkoff, The effects of ionization on the flow and heat transfer of a dense gas in a transverse electric field, *Proc. 1964 Heat Transfer and Fluid Mech. Inst.*, pp. 260 275. Stanford University Press, Stanford (1964).
2. H. R. Velkoff, Evaluating the interaction of electrostatic fields with fluid flows, Paper No. 71-DE-41, American Society of Mechanical Engineers (1970).
3. B. R. Lazarenko, F. P. Grous and M. K. Bologa, Convective heat transfer enhancement by electric fields, *Int. J. Heat Mass Transfer* **18,** 1433–1441 (1975).
4. M. E. Franke, Effect of vortices induced by corona discharge on free-convection heat transfer from a vertical plate, *J. Heat Transfer* **91,** 427–431 (1969).
5. F. A. Kulacki, S. Boriah and S. A. Martin, Corona discharge augmentation of the catalytic combustion of hydrogen in the diffusion controlled regime, *Int. J. Hydrogen Energy* **6,** 73–95 (1981).
6. J. H. Davidson, F. A. Kulacki and P. F. Dunn, Convective heat transfer with electric and magnetic fields. In *Handbook of Single-phase Convective Heat Transfer* (Edited by S. Kakac, R. Shah and W. Aung), Chap. 3. Wiley, New York (1987).
7. A. Yabe, Y. Mori and K. Hijikata, EHD study of the corona wind between wire and plate electrodes, *AIAA J.* **16,** 340–345 (1978).
8. S. Zia, Electrohydrodynamic heat transfer enhancement of forced convection in tubes, M.S. thesis, Michigan Technological University, Houghton, Michigan (1989).
9. M. E. Franke and K. E. Hutson, Effects of corona discharge on free-convection heat transfer inside a vertical hollow cylinder, *J. Heat Transfer* **106,** 346–351 (1984).
10. T. Mizushina, H. Ueda, T. Matsumoto and K. Waga, Effect of electrically induced convection on heat transfer of air flow in an annulus, *J. Chem. Engng Japan* **9,** 97–102 (1976).
11. T. Fujino, Y. Yokoyama and Y. H. Mori, Augmentation of laminar forced convection heat transfer by application of a transverse electric field, *J. Heat Transfer* **111,** 345–351 (1989).
12. A. Yabe, T. Taketani, K. Kikuchi, Y. Mori and H. Maki, Augmentation of condensation heat transfer by applying electro-hydro-dynamical pseudo-drop wise condensation, *Proc. Eighth Int. Heat Transfer Conf.*, Vol. 6, pp. 2957–2962 (1986).
13. J. S. Chang, F. Tran, K. Brunner and S. Ogata, Electric natural convection heat transfer phenomena in a heat exchanging system, *IEEE Conf. Record Industry Appl. Soc.*, pp. 1052–1058 (1981).
14. P. Cooper and P. H. G. Allen, The senftleben effect—chance or chimera? *Electron. Pwr* **30,** 807–809 (1984).
15. P. Cooper and P. H. G. Allen, The potential of electrically enhanced condensers, *Proc. 2nd Int. Symp. on Large-scale Applic. of Heat Pumps*, New York, pp. 295–309 (1984).
16. R. Poulter and I. A. Miller, Heat transfer enhancement in shell/tube heat exchangers employing electrostatic fields, *Proc. 1st U.K. Natn. Heat Transfer Conf.*, Leeds, Vol. 2, pp. 707–716 (1984).
17. R. Poulter and P. H. G. Allen, Electrohydrodynamically augmented heat and mass transfer in the shell/tube heat exchanger, *Proc. Eighth Int. Heat Transfer Conf.*, Vol. 6, pp. 2963–2968 (1986).
18. S. J. Kline and F. A. McClintock, Describing uncertainties in single-sample experiments, *Mech. Engng* **75,** 3–8 (1953).
19. B. Metais and E. R. G. Eckert, Forced, mixed, and free convection regimes, *J. Heat Transfer* 295–296 (1964).
20. R. A. Moss and J. Gray, Heat transfer augmentation by steady and alternating electric fields, *Proc. 1966 Heat Transfer and Fluid Mech. Inst.* (Edited by W. H. Giedt and S. Levy), pp. 210–235. Stanford University Press, Stanford (1966).

ACCROISSEMENT DU TRANSFERT THERMIQUE DES ECOULEMENTS LAMINAIRE OU TURBULENT DANS UN TUBE PAR DECHARGE CORONA

Résumé—On étudie expérimentalement l'effet de la décharge dans un tube. Les résultats sont rapportés pour les paramètres suivants: nombre de Reynolds (1000–15 000), potentiel de champ électrique (0 kV jusqu'au potentiel de décharge) et nombre d'électrodes (configuration à simple ou double électrode). Le fluide de travail est l'air. On trouve que l'accroissement de transfert thermique est significatif seulement dans les régimes laminaires et de transition quand on utilise une seule électrode. Avec une configuration à deux électrodes, les accroissements s'étendent au régime turbulent. A puissance de pompage constant, les accroissements sont généralement associés à la configuration à double électrode. La seule exception est pour le laminaire aux potentiels de champ le plus élevé, quand les résultats avec une seule électrode dépassent ceux avec l'électrode double.

VERBESSERUNG DES WÄRMEÜBERGANGS BEI LAMINARER UND TURBULENTER ROHRSTRÖMUNG DURCH CORONA-ENTLADUNG

Zusammenfassung—Der Einfluß einer Corona-Entladung auf den Wärmeübergang in erzwungener Konvektion in einem Rohr wird experimentell untersucht. Folgende Einflußgrößen werden variiert: Die Reynolds-Zahl (1000–15 000), das elektrische Potential (0 kV bis beinahe hin zum Spitzenentladungspotential) und die Anzahl der Elektroden (Einzel- oder Doppelelektrodenanordnungen). Bei allen Versuchen dient Luft als Arbeitsfluid. Es zeigt sich, daß eine deutliche Verbesserung des Wärmeübergangs bei Verwendung einer Einzelelektrode nur im laminaren und im Übergangsgebiet der Strömung zu beobachten ist. Bei Verwendung einer Doppelelektrodenanordnung wird auch eine Verbesserung im Bereich turbulenter Strömung erreicht. Bei konstanter Gebläseleistung ergibt die Doppelelektrodenanordnung stets die stärkere Verbesserung. Die einzige Ausnahme stellt der Fall vollständig laminarer Strömung bei höchsten Potentialen dar—hier übertreffen die Ergebnisse der Einzelelektrode diejenigen der Doppelelektrode.

ИНТЕНСИФИКАЦИЯ ТЕПЛОПЕРЕНОСА ПОСРЕДСТВОМ КОРОННОГО РАЗРЯДА ПРИ ЛАМИНАРНОМ ИЛИ ТУРБУЛЕНТНОМ ТЕЧЕНИЯХ В ТРУБАХ

Аннотация—Экспериментально исследуется влияние коронного разряда на вынужденноконвективный теплоперенос в трубе. Приводятся результаты для параметрических значений числа Рейнольдса (1000–15 000), потенциала электрического поля (от нуля до напряжения искрового пробоя) и количества электродов (одно- или двухэлектродная конфигурация). Во всех экспериментах рабочей средой является воздух. Найдено, что существенная интенсификация теплопереноса происходит только при ламинарном или переходном режимах течения, когда используется единичный электрод. В случае же конфигурации из двух электродов теплоперенос усиливается также и при турбулентном режиме. При постоянной мощности более значительная интенсификация теплопереноса достигается при двухэлектродной конфигурации. Единственным исключением является случай, когда при числах Рейнольдса, соответствующих ламинарному потоку, и максимальных потенциалах поля результаты, полученные для единичного электрода, превышают значения для парных электродов.